

# Analysis of surface emitting distributed-feedback quantum cascade laser based on a surface-plasmon waveguide\*

Guo Wanhong(郭万红), Lu Quanyong(陆全勇), Liu Junqi(刘俊岐)<sup>†</sup>, Zhang Wei(张伟),  
Jiang Yuchao(江宇超), Li Lu(李路), Wang Lijun(王利军),  
Liu Fengqi(刘峰奇), and Wang Zhanguo(王占国)

(Key Laboratory of Semiconductor Materials Science, Institute of Semiconductors,  
Chinese Academy of Sciences, Beijing 100083, China)

**Abstract:** An analysis of a surface emitting distributed-feedback quantum cascade laser (DFB QCL) based on a surface-plasmon waveguide is presented. The second-order grating realized by the sole patterning of the top metal provides strong feedback. The analysis is based on a coupled-mode theory derived from exact Floquet–Bloch solutions of the infinite periodic structure. The surface outcoupling efficiency and threshold gain for the optimized device design are 43% and  $12 \text{ cm}^{-1}$ , respectively, which represent great improvements on the conventional dielectric waveguide based DFB QCL with typical values of 17.5% and  $20 \text{ cm}^{-1}$ .

**Key words:** quantum cascade laser; distributed feedback lasers; surface plasmon waveguide; surface emission

**DOI:** 10.1088/1674-4926/31/11/114014

**EEACC:** 4255P; 4280F; 6120J

## 1. Introduction

The quantum cascade laser (QCL)<sup>[1]</sup> has proved to be a very promising light source for chemical sensing and pollution monitoring in the mid- and far-infrared wavelength regions. For many of these applications, single-mode operation and surface emission are simultaneously desirable, which can typically be realized by incorporating second-order distributed feedback (DFB) gratings<sup>[2–5]</sup> or a photonic crystal (PhC) technique into QCLs. However, the fabrication of a PhC lattice requires a deep etching technique with a high aspect ratio and precise control of the air filling factor<sup>[6]</sup>, or careful design of the side absorber<sup>[7, 8]</sup>, which are technologically challenging in the device preparation. Hence, the easy-to-fabricate second-order DFB QCLs, which are capable of both single-mode operation and surface emission, have drawn much attention and been extensively investigated<sup>[2–5, 9]</sup> over the last decade. In the mid-infrared QCLs, most of the second-order DFB structures have been based on the conventional dielectric waveguide, which is superior in terms of low optical losses but inferior in terms of material preparation for thick cladding layers and in deep grating etching processes. Consequently, there is a need to propose a new route for achieving high-efficiency surface emission DFB QCLs combined with simple fabrication techniques.

In this work, the surface-plasmon waveguide based surface-emitting DFB QCL is analyzed, where a thin metal-based contact layer is used instead of the thick cladding layers. The second-order grating is solely defined on the top metal and no etching into the semiconductors is required, thus simplifying the grating etching processes. The metal grating combined with the surface plasmon waveguide lead to strong feedback. A simulation technique, including the Floquet–Bloch analysis and the resulting coupled-mode theory, is used. The numerical

results show that the surface-plasmon waveguide based DFB QCL offers greater performance in terms of the surface outcoupling efficiency and the threshold gain than the traditional dielectric waveguide based structure.

## 2. Laser structure

Figure 1 shows a schematic cross section of the surface emitting DFB QCL considered in this work. The surface-plasmon waveguide structure is similar to that used previously for a Fabry–Perot cavity QCL in Ref. [10]. The active region identical to that in Ref. [11] is sandwiched between top thin contact-facilitating layers, consisting of 40-nm-thick InGaAs doped at  $1 \times 10^{17} \text{ cm}^{-3}$  and 10-nm-thick InGaAs doped at  $1 \times 10^{19} \text{ cm}^{-3}$ , and a bottom 0.5- $\mu\text{m}$ -thick InGaAs spacer layer doped at  $6 \times 10^{16} \text{ cm}^{-3}$ . The second-order silver grating is formed on the top with a metal depth of 150 nm and period  $\Lambda = \lambda_0/2n_{\text{eff}}$ , where  $n_{\text{eff}}$  is the effective optical index of the guided mode and  $\lambda_0 = 7.8 \mu\text{m}$  is the approximate resonance wavelength. The refractive indexes of the layers constituting the QCL are  $n_{\text{Ag}} = 3.35 + 57i$ ,  $n_{\text{contact,high-doped}} = 1.392 + 0.1i$ ,  $n_{\text{contact,low-doped}} = 3.393 + 5 \times 10^{-4}i$ ,  $n_{\text{active,region}} = 3.335 + 1 \times 10^{-4}i$ ,  $n_{\text{spacer}} = 3.401 + 2 \times 10^{-4}i$  and  $n_{\text{InP,substrate}} = 3.066 + 1 \times 10^{-3}i$ . Among these values, the refractive indexes for the doped semiconductor layers are calculated using a Drude–Lorentz model<sup>[12]</sup>, while the value for silver is taken from Ref. [13].

## 3. Theory

### 3.1. Floquet–Bloch solutions for the infinite-length laser structure

The analysis of a surface emitting DFB QCL based on

\* Project supported by the National Science Fund for Distinguished Young Scholars of China (No. 60525406), the National Natural Science Foundation of China (Nos. 60736031, 60806018, 60906026), the National Basic Research Program of China (No. 2006CB604903) and the National High Technology Research and Development Program of China (Nos. 2007AA03Z446, 2009AA03Z403).

<sup>†</sup> Corresponding author. Email: jqliu@semi.ac.cn

Received 25 May 2010

© 2010 Chinese Institute of Electronics

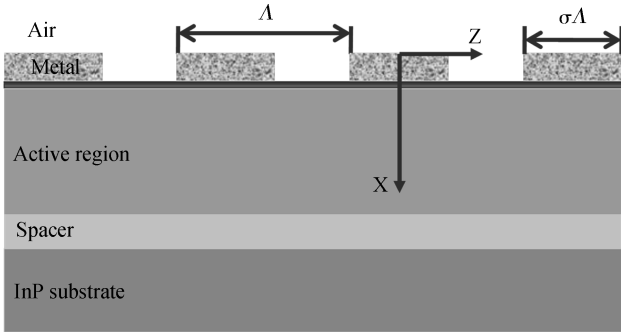


Fig. 1. Schematic cross section of the investigated laser structure.  $\Lambda$  and  $\sigma$  denote the grating period and the duty cycle, respectively.

second-order gratings begins with solving the Floquet–Bloch eigenmodes of the infinite-length laser structure numerically. Since the propagation wavevector  $2\pi n_{\text{eff}}/\lambda_0$  equals the Bragg wavevector  $2\pi/\Lambda$  satisfying the second-order Bragg condition, the mode in the infinite-length laser is in resonance with the grating. Therefore, there are two standing wave solutions, with two slightly different frequencies correspondingly, thus forming a bandgap at resonance. Here, we consider only TM-polarized modes where the magnetic field points in the  $y$  direction, as shown in Fig. 1. In the infinite-length device, the magnetic field can be written in terms of an exact Floquet–Bloch expansion, given by

$$H(x, z) = \sum_{m=0, \pm 1, \dots} H_m(x)e^{imKz}, \quad (1)$$

where  $K = 2\pi/\Lambda$  is the grating vector. In this expression,  $H_0$  describes the surface emission field. The partial waves  $H_m$  are found to satisfy the following complex eigenvalue equations<sup>[14]</sup>,

$$\frac{d^2 H_m}{dx^2} = \sum_p \left\| \frac{1}{\varepsilon} \right\|_{mp}^{-1} \sum_q \left( pqK^2 \|\varepsilon\|_{pq}^{-1} - k^2 \delta_{pq} \right) H_q \quad (2)$$

where  $\|f\|$  denotes the Toeplitz matrix generated by the Fourier coefficients of  $f$ , such that its  $(p, q)$  entry is  $f_{p-q}$ ,  $\varepsilon$  is the dielectric function,  $\delta_{pq}$  is the Kronecker symbol,  $-1$  denotes the matrix inverse and  $k = 2\pi/\lambda$  is the free-space wave vector at the wavelength  $\lambda$  of the resonance. The above eigenequation is solved under the continuity conditions and the radiation boundary conditions, yielding two eigenmodes with field patterns that are symmetric and anti-symmetric with respect to the grating. The corresponding eigenvalues are  $k_s$  and  $k_{as}$ , respectively, corresponding to the two resonant band-edge modes.

### 3.2. Coupled-mode theory for the finite-length laser structure

For the finite-length device, the magnetic field can be written approximately as a linear combination of the two resonant band-edge modes of the infinite-length grating<sup>[15]</sup>. The corresponding amplitudes, denoted by  $R$  and  $S$ , represent  $z$ -dependent amplitudes of the forward and backward waves, respectively. These amplitudes can be described by the classic coupled-wave equations<sup>[16]</sup>, which are given by

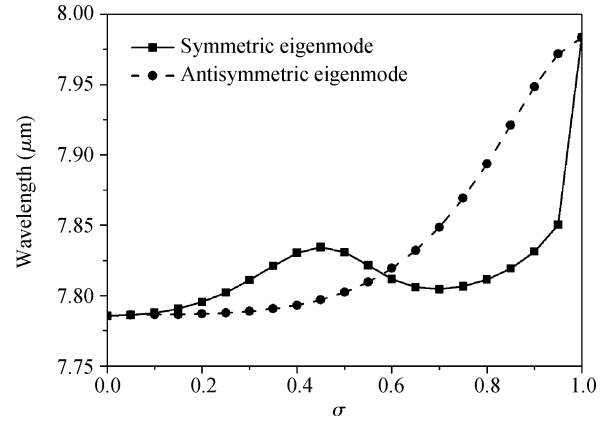


Fig. 2. Eigenmode wavelength as a function of the grating duty cycle  $\sigma$  for the infinite-length device structure.

$$\begin{aligned} \frac{dS}{dz} + (-\alpha + i\zeta + i\delta)S &= i\kappa R, \\ -\frac{dR}{dz} + (-\alpha + i\zeta + i\delta)R &= i\kappa S. \end{aligned} \quad (3)$$

Here,  $\alpha$  is the field gain coefficient at threshold and  $\delta$  denotes the normalized frequency. The coupling coefficients  $\zeta$  and  $\kappa$  are related to the eigenvalues of the infinite-length device by<sup>[15]</sup>

$$\begin{aligned} \zeta &= -\frac{(k_s + k_{as} - 2k_0) K}{2k_0} - \frac{(\alpha_s + \alpha_{as})}{2}i, \\ \kappa &= \frac{(k_s - k_{as}) K}{2k_0} + \frac{(\alpha_s - \alpha_{as})}{2}i, \end{aligned} \quad (4)$$

where  $k_0 = 2\pi/\lambda_0$  is the approximate resonance wavevector, and  $\alpha_s$  ( $\alpha_{as}$ ) are the waveguide losses for the symmetric (anti-symmetric) eigenmode calculated for the infinite-length structure. Once  $\zeta$ ,  $\kappa$  and the device length  $L$  are given, the threshold power gain coefficient  $g_{\text{th}}$  and surface outcoupling efficiency  $\eta_{\text{surf}}$  can be obtained by solving the above coupled-wave equations. The detailed algorithm can be found in our previous work<sup>[17]</sup>.

## 4. Results and discussion

### 4.1. Loss and coupling coefficients

To numerically investigate the influence of the device parameters, such as the grating duty cycle  $\sigma$  and the device length  $L$  on the device performance, it is necessary to analyze infinite-length device structure first. The period of the second-order grating is  $\Lambda = 2.43 \mu\text{m}$  with the effective index  $n_{\text{eff}} = 3.21$ . The behavior of the eigenmode of the infinite-length structure at various duty cycles is shown in Fig. 2, where the crossing of the curves indicates a switching of the symmetric and anti-symmetric eigenmodes. Figure 3 shows the numerically calculated magnetic field for the symmetric and anti-symmetric eigenmodes with duty cycle  $\sigma = 0.5$ . In the anti-symmetric eigenmode, both positive and negative lobes appear between the teeth of the grating. This causes destructive interference outside the grating, and consequently the anti-symmetric eigenmode does not radiate<sup>[14]</sup>. For the symmetric

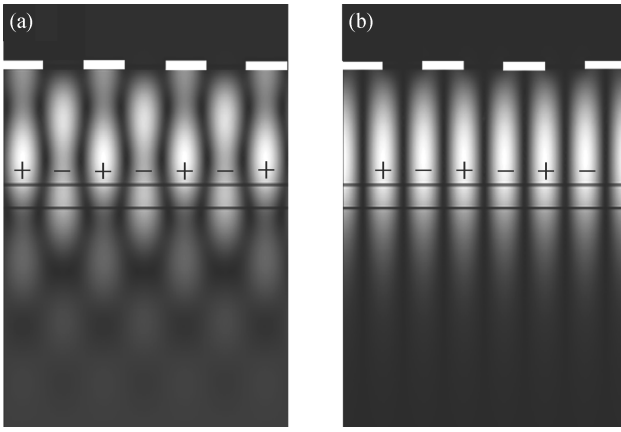


Fig. 3. Magnetic field of (a) symmetric and (b) anti-symmetric modes for the infinite-length structure with  $\sigma = 0.5$ .

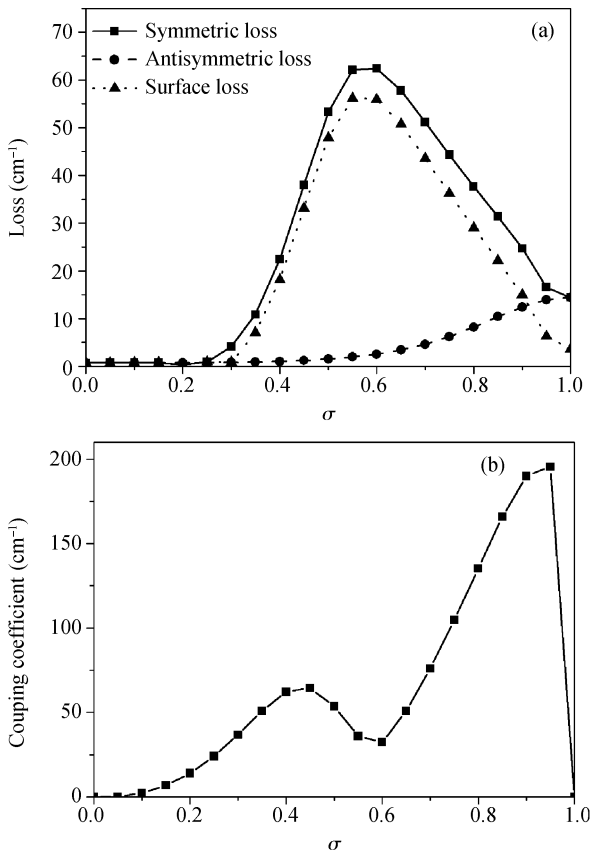


Fig. 4. (a) Waveguide loss coefficients and (b) coupling coefficient versus duty cycle  $\sigma$ .

eigenmode, only positive lobes appear. There is no interference, and the radiating component is non-zero. Therefore, there is higher loss in the symmetric eigenmode due to the introduction of the surface radiation loss.

Figure 4 depicts the behaviors of the losses and coupling coefficients with varying duty cycles. From Fig. 4(a), when  $\sigma$  is less than 0.2, the waveguide losses of both symmetric and anti-symmetric eigenmodes are extremely small. This is due to a small overlap of the grating and the optical mode. As  $\sigma$  rises, the portion of propagation loss of surface plasmon mode gradually increases, which contributes to the enhancement of the

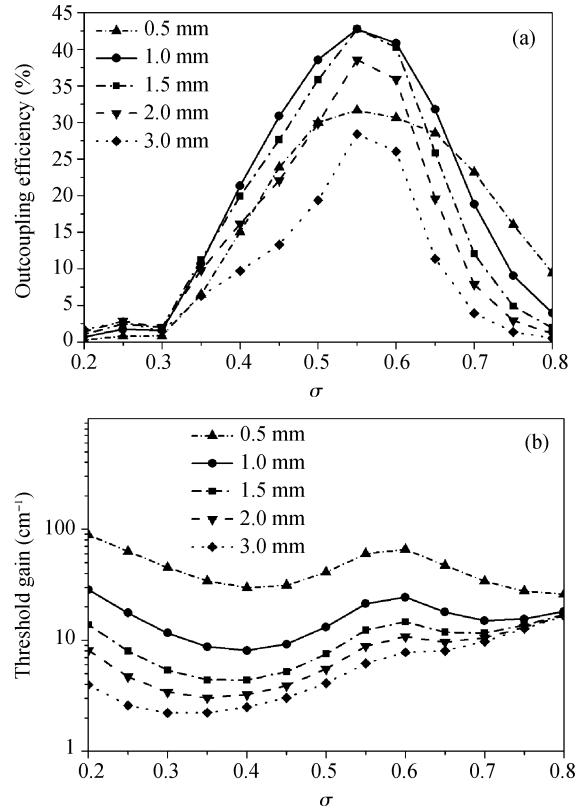


Fig. 5. (a) Surface outcoupling efficiency  $\eta_{\text{surf}}$  and (b) threshold gain  $g_{\text{th}}$  versus duty cycle  $\sigma$  for  $L = 0.5, 1.0, 1.5, 2.0$  and  $3.0$  mm.

waveguide loss of the anti-symmetric eigenmode. Meanwhile, both the surface loss and the waveguide loss for the symmetric eigenmode reach their peaks near  $\sigma = 0.5$ . Therefore, it is necessary to maximize the fraction of the symmetric eigenmode to design the device with high surface outcoupling efficiency, due to its large surface loss. Figure 4(b) shows the coupling coefficient as a function of the grating duty cycle. Compared with the dielectric-waveguide based grating with typical values in the range  $4\text{--}7\text{ cm}^{-1}$ [4], the coupling coefficients for the surface plasmon-based structure are much larger, which can be attributed to large mode overlap with the metal grating and the strong complex index contrast.

#### 4.2. Threshold gain and outcoupling efficiency

The threshold gain  $g_{\text{th}}$  and the surface outcoupling efficiency  $\eta_{\text{surf}}$  depend strongly on the grating duty cycle  $\sigma$  and the device length  $L$ . Figures 5(a) and 5(b) show  $g_{\text{th}}$  and  $\eta_{\text{surf}}$  as a function of  $\sigma$  for different  $L$ . We found that the curves for different device lengths have similar trends with varying  $\sigma$ . For small duty cycles ( $\sigma < 0.3$ ),  $\eta_{\text{surf}}$  displays small values. This is caused by the small overlap of the optical mode with the grating, i.e., a little fraction of metal attracts a small portion of optical field into the grating region. As  $\sigma$  increases, the mode-grating overlapping and thus  $\eta_{\text{surf}}$  enhances till the latter reaches a maximum at  $\sigma = 0.55$ . For higher duty cycles ( $\sigma > 0.7$ ),  $\eta_{\text{surf}}$  decreases because the increasing overlap is jeopardized by the fact that the perturbation of the refractive index is getting smaller. On the other hand,  $g_{\text{th}}$  is very high for small duty cycles because of the fact that the optical mode is not effectively confined to the active region by a little fraction of

Table 1. Refractive indexes of metals along with loss and coupling coefficients, as well as the optimal surface outcoupling efficiency and threshold gain. The surface emitting DFB QCL operates at a wavelength of 7.8  $\mu\text{m}$ . The refractive indexes of metals are cited from Ref. [13].

Metal	$n$	$\alpha_s$ ( $\text{cm}^{-3}$ )	$\alpha_{as}$ ( $\text{cm}^{-3}$ )	$\alpha_s^{\text{surf}}$ ( $\text{cm}^{-3}$ )	$K$ ( $\text{cm}^{-3}$ )	$\eta_{\text{surf}}$ (%)	$g_{\text{th}}$ ( $\text{cm}^{-3}$ )
Silver	$3.35 + 57i$	62.14	1.93	56.20	35.95	42.74	12.32
Gold	$7.78 + 57i$	62.40	2.03	48.60	36.73	33.83	15.17
Palladium	$3.13 + 36i$	68.15	2.12	46.10	36.14	32.27	12.98

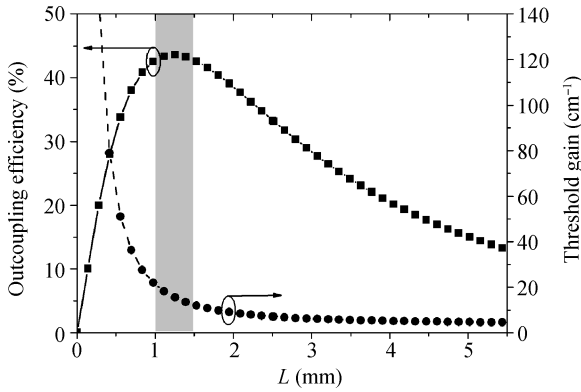


Fig. 6. Surface outcoupling efficiency and threshold gain versus device length  $L$ , with  $\sigma = 0.55$  used in the calculation.

metal. In addition,  $g_{\text{th}}$  displays a high value at  $\sigma = 0.6$  induced by a large surface loss. Consequently, to achieve a high value of  $\eta_{\text{surf}}$  as well as a small  $g_{\text{th}}$ , the optimal value of  $\sigma$  ought to be in the range of 0.5–0.6. Also, from Fig. 5(a), one can find that  $\eta_{\text{surf}}$  for devices with different lengths reaches the maximum value at the same duty cycle  $\sigma = 0.55$ . At this point,  $\eta_{\text{surf}}$  for a 1.5-mm-length device is equal to that for a 1.0-mm-length device, higher than for devices with smaller or larger lengths.

In the following, the effect of device length  $L$  on device performance is thoroughly examined. As shown in Fig. 6, at short device lengths, the grating provides only little feedback, which results in a higher threshold gain  $g_{\text{th}}$  caused by a higher facet loss and lower surface outcoupling efficiency  $\eta_{\text{surf}}$ . At large device lengths,  $g_{\text{th}}$  approaches a constant determined by the absorption loss with increasing  $L$ , and  $\eta_{\text{surf}}$  also decreases because the optical intensity is mainly concentrated in the center of the device<sup>[16]</sup>, resulting in only a small portion of power perpendicularly diffracted into the air. In contrast, at intermediate device lengths,  $\eta_{\text{surf}}$  displays a large value of 40%–43% due to a uniform power distribution in the device. Consequently, the optimized value of device length is in the range 1.0–1.5 mm, as indicated in the gray area in Fig. 6, while the corresponding  $g_{\text{th}}$  still maintains a relatively small value between 11 and 22  $\text{cm}^{-1}$ . In this paper, the highest surface outcoupling efficiency of 43% with a low threshold gain of 12  $\text{cm}^{-1}$  is obtained with an optimal device length of 1.25 mm. These optimal results show a dramatic improvement compared with typical results for a dielectric-waveguide based surface emitting DFB QCL with a surface outcoupling efficiency of 17.5% and a threshold gain of 20  $\text{cm}^{-1}$ <sup>[9]</sup>.

Although a silver-based surface-plasmon waveguide is adopted in the above device design, other typical metals, such as gold and palladium, are commonly used as the surface-plasmon guiding layer in the mid-infrared wavelength region as well. Therefore, for comparison, similar optimal computa-

tion procedures were performed using gold and palladium instead of silver. The results are summarized in Table 1, where the effect of these metals on the loss as well as the coupling coefficients, and therefore the device performance, are shown. From this table, we found that the waveguide loss and coupling coefficients for devices utilizing these three kinds of metals have no significant differences, and thus their threshold gains do not differ much. However, as for surface loss, silver has a larger value than the other two metals, and therefore a larger surface outcoupling efficiency. Consequently, among the above three metals, silver is the optimal choice for the metal surface-plasmon guiding layer for a surface emitting DFB QCL near 7.8  $\mu\text{m}$ .

### 5. Conclusion

We have analyzed a surface emitting DFB QCL based on a surface-plasmon waveguide, utilizing a coupled-mode theory derived from exact Floquet–Bloch solutions of infinitely periodic structure. The distributed feedback is achieved via a second-order grating in the sole patterning of the top metal. Simulations show a strong dependence of device performance on the grating duty cycle and the device length. An optimized device design, with a surface outcoupling efficiency of 43% and a threshold gain of 12  $\text{cm}^{-1}$ , is obtained, which is dramatically superior to the conventional dielectric waveguide based DFB QCL. These results indicate that the surface-plasmon based surface-emitting DFB QCL is a good alternative to the conventional dielectric-waveguide based structure.

### References

- [1] Faist J, Capasso F, Sivco D L, et al. Quantum cascade laser. *Science*, 1994, 264: 553
- [2] Hofstetter D, Faist J, Beck M, et al. Surface-emitting 10.1  $\mu\text{m}$  quantum-cascade distributed feedback lasers. *Appl Phys Lett*, 1999, 75: 3769
- [3] Schrenk W, Finger N, Gianordoli S, et al. Surface-emitting distributed feedback quantum-cascade lasers. *Appl Phys Lett*, 2000, 77: 2086
- [4] Pflugl C, Austerer M, Schrenk W, et al. Single-mode surface-emitting quantum-cascade lasers. *Appl Phys Lett*, 2005, 86: 211102
- [5] Schartner S, Austerer M, Schrenk W, et al. Surface emission from episcide-down short distributed-feedback quantum cascade lasers. *Opt Express*, 2008, 16: 11920
- [6] Colombelli R, Srinivasan K, Troccoli M, et al. Quantum cascade surface-emitting photonic crystal laser. *Science*, 2003, 302: 1374
- [7] Chassagneux Y, Colombelli R, Maineult W, et al. Electrically pumped photonic-crystal terahertz lasers controlled by boundary conditions. *Nature*, 2009, 457: 174
- [8] Xu G, Moreau V, Chassagneux Y et al. Surface-emitting quantum cascade lasers with metallic photonic-crystal resonators. *Appl*

- Phys Lett, 2009, 94: 221101
- [9] Finger N, Schrenk W, Gornik E. Analysis of TM-polarized DFB laser structures with metal surface gratings. *IEEE J Quantum Electron*, 2000, 36: 780
- [10] Tredicucci A, Gmachl C, Wanke M C, et al. Surface plasmon quantum cascade lasers at  $\lambda \approx 19 \mu\text{m}$ . *Appl Phys Lett*, 2000, 77: 2286
- [11] Wittmann A, Giovannini M, Faist J, et al. Room temperature continuous wave operation of distributed feedback quantum cascade lasers with widely spaced operation frequencies. *Appl Phys Lett*, 2006, 89: 141116
- [12] Scarpa G, Ulbrich N, Bohm G, et al. Low-loss GaInAs-based waveguides for high-performance  $5.5 \mu\text{m}$  InP-based quantum cascade lasers. *IEE Proc Optoelecton*, 2003, 150(4): 284
- [13] Bahriz M, Moreau V, Palomo J, et al. Room-temperature operation of  $\lambda \approx 7.5 \mu\text{m}$  surface-plasmon quantum cascade lasers. *Appl Phys Lett*, 2006, 88: 181103
- [14] Schubert M, Rana F. Analysis of Terahertz surface emitting quantum-cascade lasers. *IEEE J Quantum Electron*, 2006, 42(3): 257
- [15] Noll R J, Macomber S H. Analysis of grating surface emitting lasers. *IEEE J Quantum Electron*, 1990, 26(3): 456
- [16] Kogelnik H, Shank C V. Coupled-wave theory of distributed feedback lasers. *J Appl Phys*, 1972, 43: 2327
- [17] Guo Wanhong, Liu Junqi, Lu Quanyong, et al. Design of surface emitting distributed feedback quantum cascade laser with single-lobe far-field pattern and high outcoupling efficiency. *Chinese Physics B*, 2010, 19(5): 054208